Supplementary Information

Ultrahigh Mobility and Rashba Spin Splitting in Sb-substituted Bismuth Telluride and Bismuth Selenide

R. Kavkhani[1], B. Akgenc Hanedar[2, 3], K. Anar[1] , A. İ. Şahin[1] , A. Johansson[4,5], and M. C. Onbaşlı[3,6]

[1]Graduate School of Sciences and Engineering (GSSE), Koç University, Rumelifeneri Yolu, Sarıyer 34450 Istanbul, Türkiye
[2]Department of Physics, Kirklareli University, Kirklareli, 39100, Türkiye
[3]Department of Physics, Koç University, Rumelifeneri Yolu, Sarıyer 34450 Istanbul, Türkiye
[4]Max Planck Institute of Microstructure Physics, Weinberg 2, 06120 Halle (Saale), Germany
[5]Halle-Berlin-Regensburg Cluster of Excellence CCE, Germany
[6]Department of Electrical & Electronics Engineering, Koç University, Rumelifeneri Yolu, Sarıyer 34450 Istanbul, Türkiye

*Corresponding author: berna.akgenc@klu.edu.tr; monbasli@ku.edu.tr

1. Selection of the Most Stable Atomic Configuration

As summarized in Table S1, for each doping level, the configuration with the lowest formation energy was selected to ensure structural stability and physical relevance in subsequent analyses. This lowest-energy configuration was subsequently employed for all further calculations, including electronic structure.

Table S1. Formation energies (eV/atom) of $(Bi_{1-x}Sb_x)_2Te_3$ for three configurations at different Sb contents.

Compound	E_{for} **Config.1 (eV)**	E_{for} **Config.2 (eV)**	E_{for} **Config.3 (eV)**
$(Bi_{0.5}Sb_{0.5})_2Te_3$	−0.27055	−0.27061	−0.27022
$(Bi_{0.4}Sb_{0.6})_2Te_3$	−0.25732	−0.25737	−0.25720
$(Bi_{0.1}Sb_{0.9})_2Te_3$	−0.21598	−0.21599	−0.21597

2. Analysis of the Edelstein Tensor and Transport Parameters for $(Bi_{1-x}Sb_x)_2Te_3$

The Edelstein tensor χ_{ij} quantifies how an electric field applied to a material with spin–orbit coupling induces a net spin density,

$$S_i = \chi_{ij} E_j, \tag{1}$$

where S_i is the spin density and E_j is the applied electric field. For a two-dimensional Rashba system, the Edelstein tensor has the form

$$\boldsymbol{\chi} = \begin{pmatrix} 0 & \chi_{xy} & 0 \\ \chi_{yx} & 0 & 0 \\ 0 & 0 & 0 \end{pmatrix}, \qquad \chi_{xy} = -\chi_{yx}. \tag{2}$$

The calculated Edelstein tensor components (in units of $\mathrm{m}^{-1}\,\mathrm{V}^{-1}$) are as follows. For $(Bi_{0.1}Sb_{0.9})_2Te_3$ (BST-90) with effective mass $m^* = 0.13m_e$ and Rashba parameter $\alpha_R = 0.719$,

$$\chi_{xy} = 4.2150 \times 10^5, \qquad \chi_{yx} = -4.2150 \times 10^5. \tag{3}$$

For $(Bi_{0.4}Sb_{0.6})_2Te_3$ with effective mass $m^* = 0.054m_e$ and Rashba parameter $\alpha_R = 2.098$,

$$\chi_{xy} = 9.4351 \times 10^5, \qquad \chi_{yx} = -9.4351 \times 10^5. \tag{4}$$

The small diagonal terms are negligible and arise from minor numerical mixing. The out-of-plane components ($\chi_{zx}, \chi_{zy} \approx 10^{-6}$) are nearly zero, confirming that at $\lambda_w = 0$ (no warping) the spin polarization is entirely in-plane. The magnitude of the Edelstein response increases significantly from BST-90 to BST-60. This enhancement reflects the stronger Rashba coupling at intermediate Sb concentrations, which increases both the spin–momentum locking strength and the effective Fermi surface splitting. As the Rashba splitting grows, a given electric field produces a larger nonequilibrium shift in momentum space, resulting in a correspondingly larger induced spin density.

The calculated (scalar) conductivity (in units of Siemens) is as follows.

For $(Bi_{0.1}Sb_{0.9})_2Te_3$ with $m^* = 0.13m_e$ and $\alpha_R = 0.719$,

$$\sigma = 2.59814619 \times 10^{-3}. \tag{5}$$

For $(Bi_{0.4}Sb_{0.6})_2Te_3$ with $m^* = 0.054m_e$ and $\alpha_R = 2.098$,

$$\sigma = 6.05950614 \times 10^{-3}. \tag{6}$$

The increase from BST-90 to BST-60 reflects enhanced carrier velocity and Rashba splitting at intermediate Sb concentrations.

To compute the relaxation times, we employed a Gaussian impurity-scattering model, in which the impurity potential in momentum space is given by

$$U(\mathbf{q}) = U_0 \exp\left(-\frac{q^2\xi^2}{2}\right). \tag{7}$$

In the calculations, the impurity concentration $c_{\mathrm{imp}} = 0.01$, the correlation length $\xi = 0.9 \times 10^{-9}\,\mathrm{m}$, and the potential

$$U_0(\mathbf{q}) = 0.01\, e\, A_0, \tag{8}$$

where A_0 is the unit-cell area, were used. With these parameters, the momentum-dependent scattering rate was evaluated as

$$\Gamma(\mathbf{k}) = \frac{2\pi}{\hbar}\, c_{\mathrm{imp}}\, N\, |U(\mathbf{q})|^2 \sum_{\mathbf{k}'} |\langle u_{\mathbf{k}} | u_{\mathbf{k}'} \rangle|^2 \delta(E_{\mathbf{k}} - E_{\mathbf{k}'}), \tag{9}$$

and the relaxation time was obtained from

$$\tau(\mathbf{k}) = \frac{1}{\Gamma(\mathbf{k})}. \tag{10}$$

The resulting relaxation times are:

For $(Bi_{0.1}Sb_{0.9})_2Te_3$ with $m^* = 0.13m_e$ and $\alpha_R = 0.719$:

$$\tau_{\text{outer}} = 0.214775 \times 10^{-12}\,\text{s}, \qquad \tau_{\text{inner}} = 0.208625 \times 10^{-12}\,\text{s}. \tag{11}$$

For $(Bi_{0.4}Sb_{0.6})_2Te_3$ with $m^* = 0.054m_e$ and $\alpha_R = 2.098$:

$$\tau_{\text{outer}} = 0.44850 \times 10^{-12}\,\text{s}, \qquad \tau_{\text{inner}} = 0.445600 \times 10^{-12}\,\text{s}. \tag{12}$$

The nearly identical relaxation times for the inner and outer Rashba branches indicate symmetric scattering and weak interband coupling, which is typical for moderate Rashba splitting. A relaxation time on the order of $\tau \approx 10^{-12}$ s corresponds to high mobility.

3. Dipole Moment and LDOS Analysis

The dipole moment (μ_z) was calculated using VASP with the tags `LDIPOL = .TRUE.` and `IDIPOL = 3`, which enable correction for the dipole field along the out-of-plane (z) direction. The obtained values reveal a polarity reversal at $x = 0.6$, indicating a transition from nearly centrosymmetric to non-centrosymmetric atomic configurations and confirming the development of strong structural inversion asymmetry (SIA), as shown in Table S2. The local density of states (LDOS) distribution near the Fermi level (Figure S3) similarly shows an asymmetric charge localization at $x = 0.6$. The spatial separation of electronic density across the quintuple layers further supports the existence of a built-in dipole field, consistent with the polarity reversal identified from the dipole moment analysis.

Table S2. Calculated dipole moment μ_z (e·Å) obtained from VASP using `LDIPOL = .TRUE.` and `IDIPOL = 3`.

System	μ_z **(e·Å)**	**Summary**
Bi_2Te_3	–0.0030	nearly centrosymmetric, negligible SIA
$(Bi_{0.5}Sb_{0.5})_2Te_3$	–0.0118	increasing SIA due to partial ionic imbalance
$(Bi_{0.4}Sb_{0.6})_2Te_3$	+0.0172	polarity reversal and maximum SIA, strongest Rashba splitting

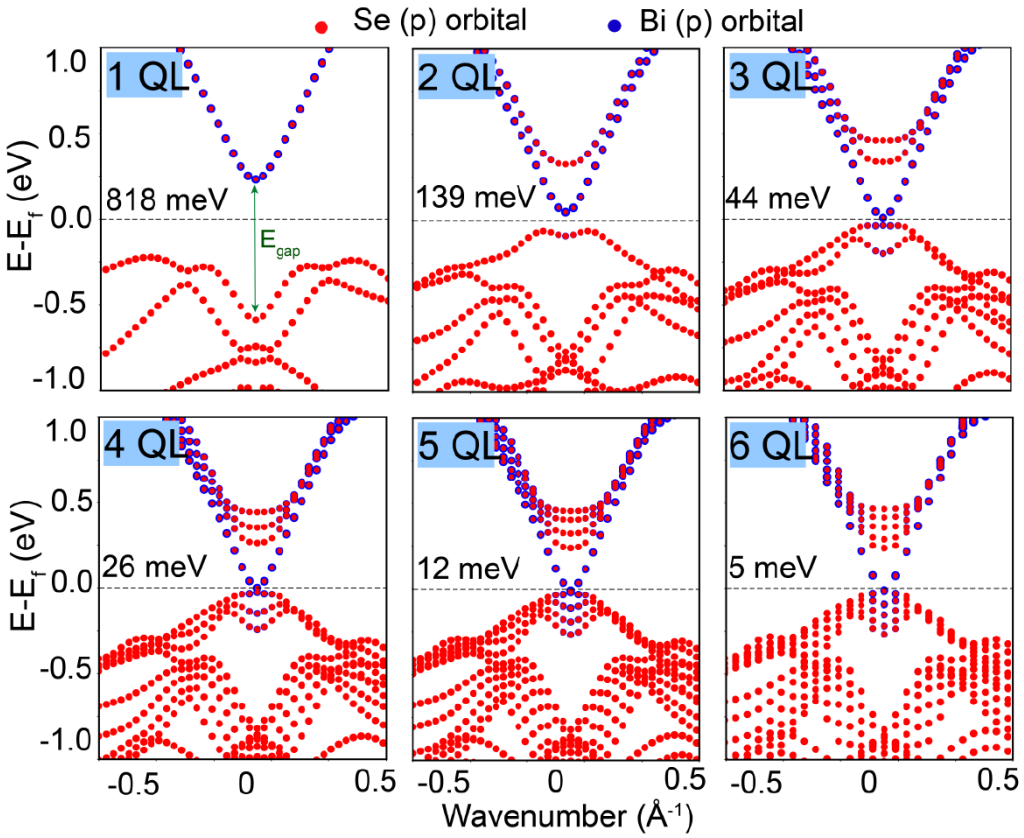

Figure S1. Thickness-dependent electronic band structures of Bi_2Se_3 from 1 to 6 QLs, projected onto Bi (blue) and Se (red) *p*-orbitals. The color intensity represents the orbital contribution to each band.

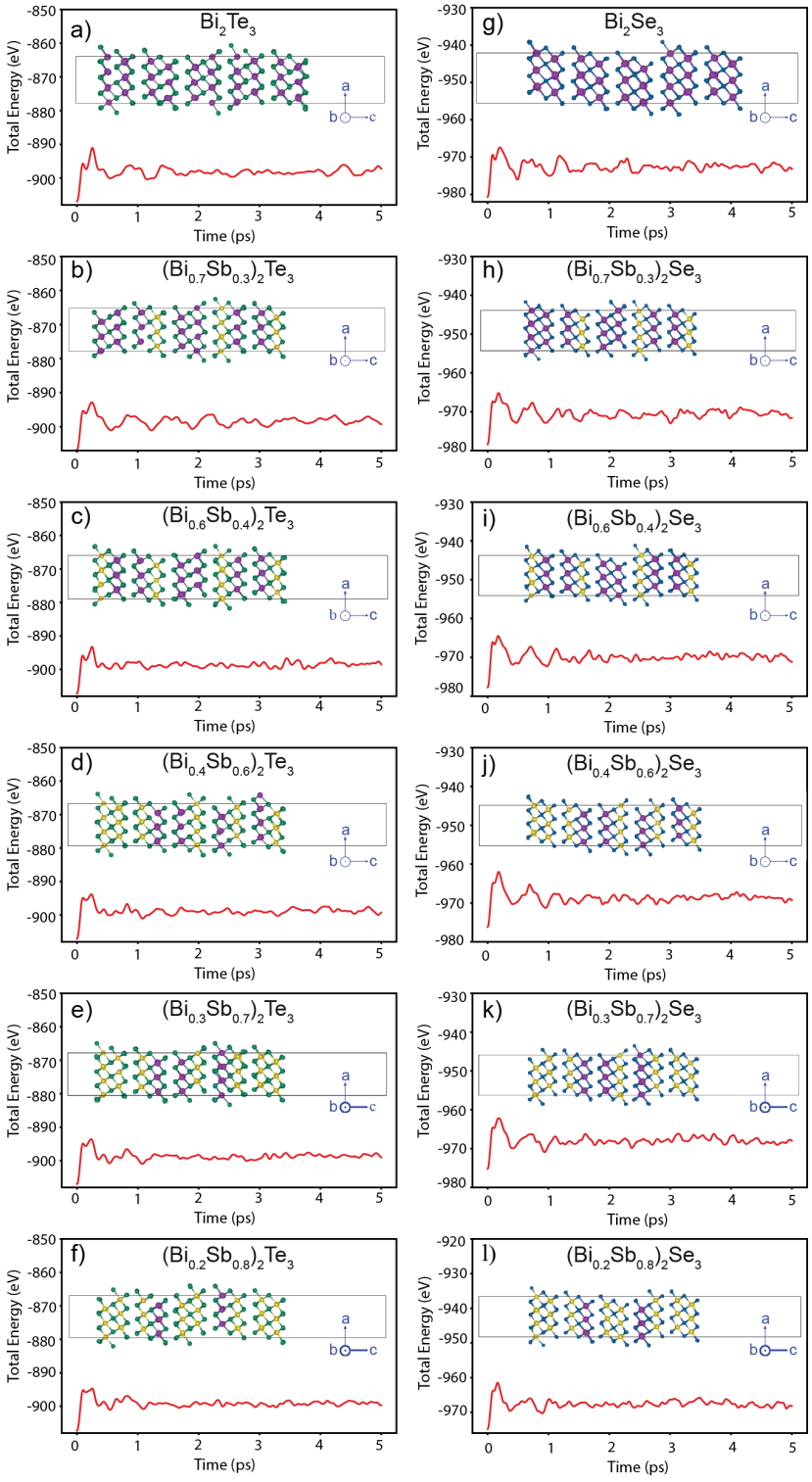

Figure S2. Ab initio molecular dynamics (AIMD) simulations performed at 300 K for various Sb doping concentrations in 5QL unit cells of $(Bi_{1-x}Sb_x)_2Te_3$ (BST) and $(Bi_{1-x}Sb_x)_2Se_3$ (BSS). Each panel shows the total energy variation over time (0–5 ps), indicating the thermal stability of the systems under room-temperature conditions. Insets display the relaxed atomic configurations after the 5 ps simulation. (a–f) correspond to BST systems with increasing Sb compositions: (a) $x = 0$, (b) $x = 0.3$, (c) $x = 0.4$, (d) $x = 0.6$, (e) $x = 0.7$, and (f) $x = 0.8$. (g–l) correspond to BSS systems with the same respective Sb compositions: (g) $x = 0$, (h) $x = 0.3$, (i) $x = 0.4$, (j) $x = 0.6$, (k) $x = 0.7$, and (l) $x = 0.8$.

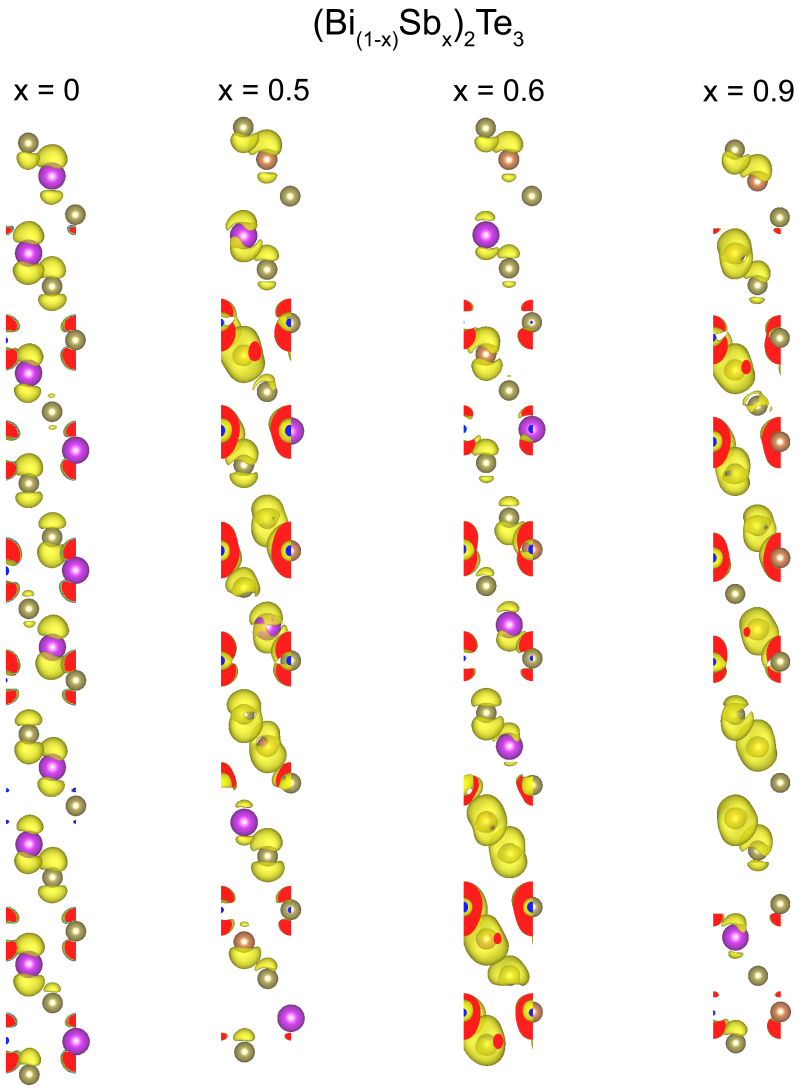

Figure S3. Local density of states (LDOS) near the Fermi level for $(Bi_{1-x}Sb_x)_2Te_3$ at different Sb compositions ($x = 0$, 0.5, 0.6, and 0.9). Yellow regions indicate electronic localization, while red areas correspond to the structural cross-sectional plane. The LDOS distributions highlight the evolution of charge localization and symmetry breaking with increasing Sb content.

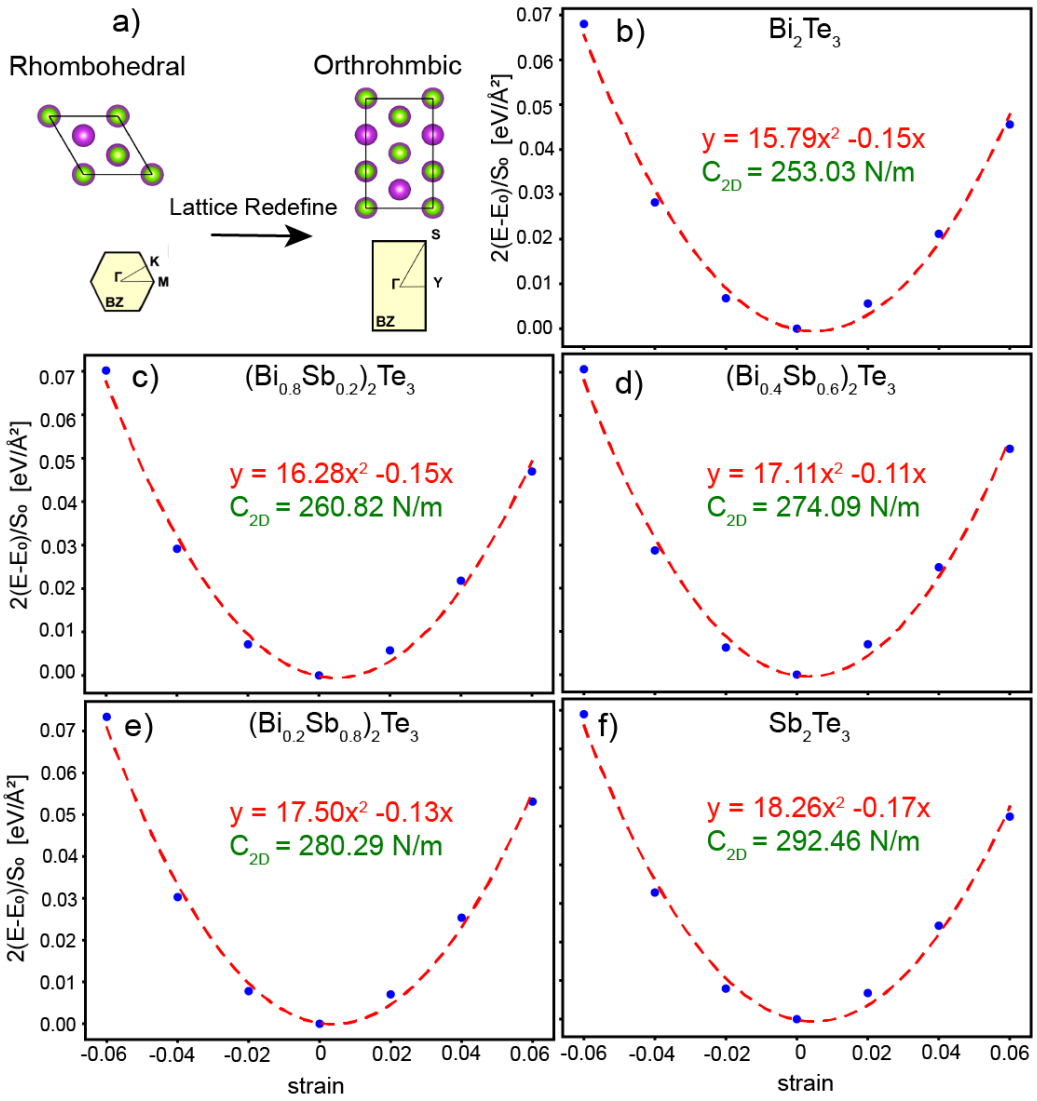

Figure S4. (a) Schematic illustration showing the change in the crystal model used for computation. (b–f) Calculated elastic modulus (C) values for the corresponding models obtained from *ab initio* calculations and polynomial fitting. The fitted curves demonstrate the strain–energy relationship and validate the mechanical stability of each configuration.

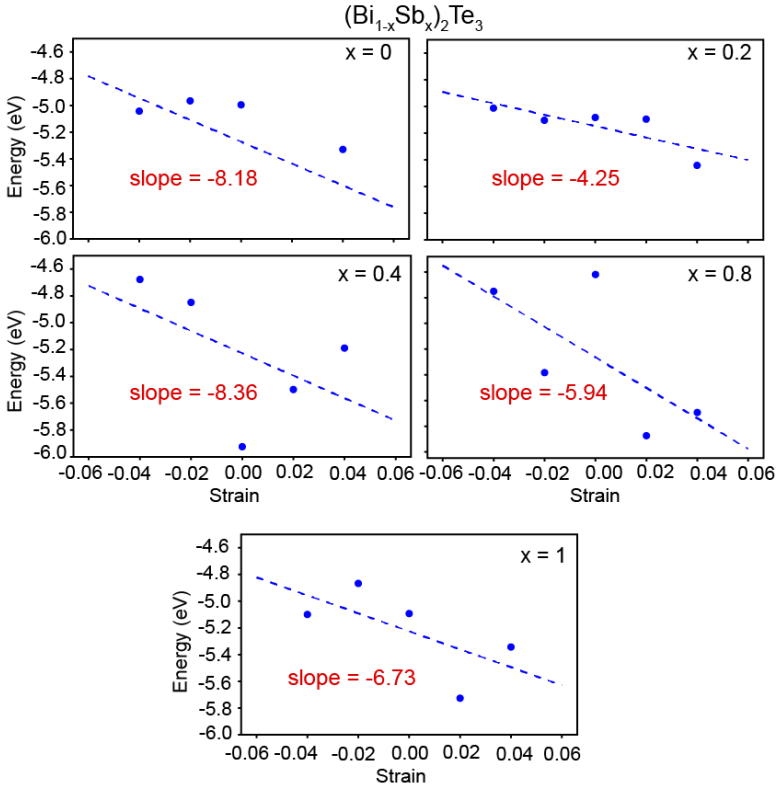

Figure S5. The deformation potential constant (E_1) was determined by fitting the variation of the conduction band minimum (CBM) energy with respect to the vacuum level as a function of applied strain for the surface states. The linear fit provides the slope corresponding to E_1, which quantifies the coupling between strain and electronic band-edge shifts in the surface region.

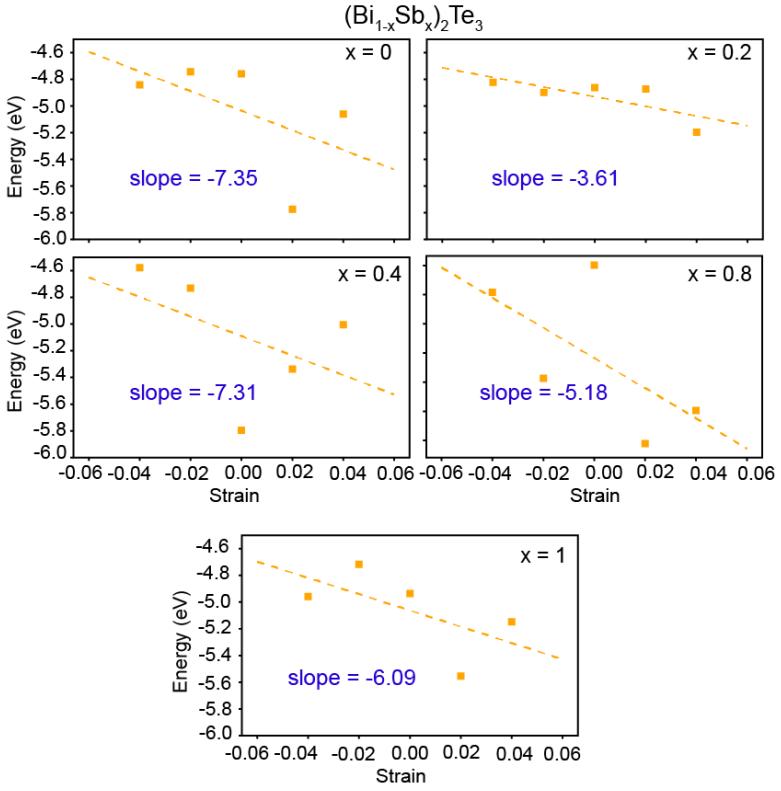

Figure S6. The deformation potential constant (E_1) for the bulk states was extracted by fitting the variation of the conduction band minimum (CBM) energy relative to the vacuum level as a function of the applied strain. The linear relationship obtained from the fitting defines the slope corresponding to E_1, representing the strength of electron–phonon coupling and strain sensitivity within the bulk region.

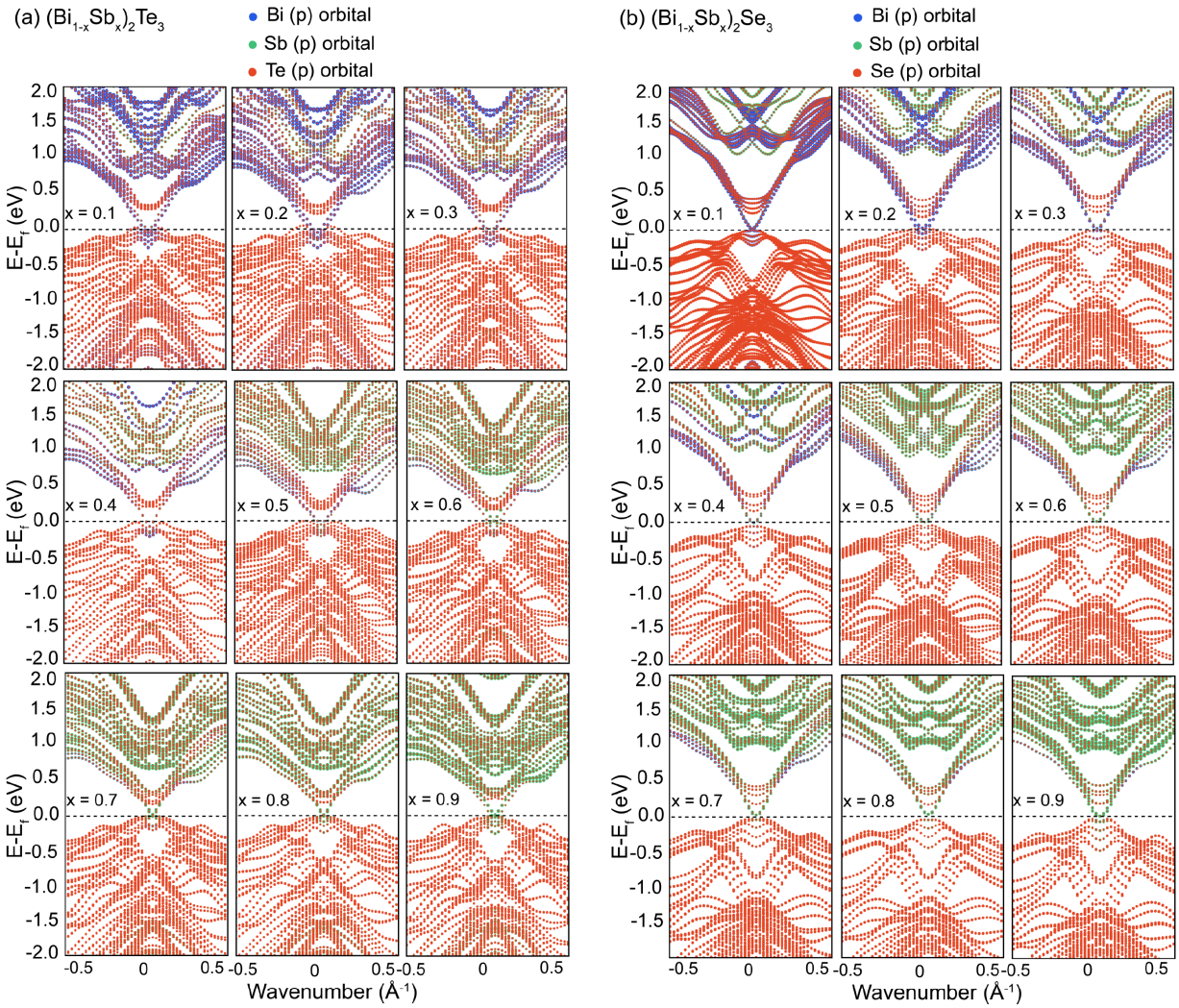

Figure S7. Orbital-projected electronic band structures of (a) $(Bi_{1-x}Sb_x)_2Te_3$ and (b) $(Bi_{1-x}Sb_x)_2Se_3$, calculated for Sb compositions ranging from $x = 0.1$ to 0.9. The orbital contributions from Bi, Sb, and Te/Se p-states are represented in blue, green, and red, respectively. The progressive evolution of the bands with increasing x highlights the modification of spin–orbit coupling strength and band inversion behavior across the substitution range.

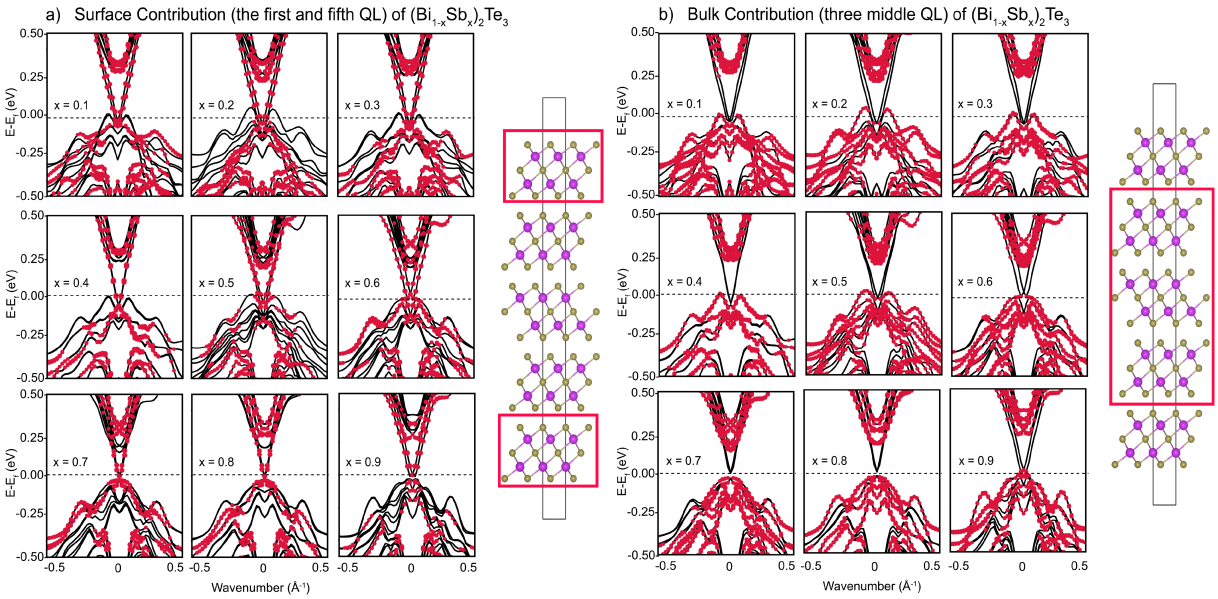

Figure S8. Orbital-weighted band structures of $(Bi_{1-x}Sb_x)_2Te_3$ for Sb compositions ranging from $x = 0.1$ to 0.9 in increments of 0.1. (a) Surface contributions originating from the top and bottom QLs. (b) Bulk contributions derived from the three central QLs. Red dots highlight the states with dominant surface or bulk character, as schematically depicted on the right. The evolution of these states across increasing x reflects the transition between surface-dominated and bulk-dominated electronic behavior.

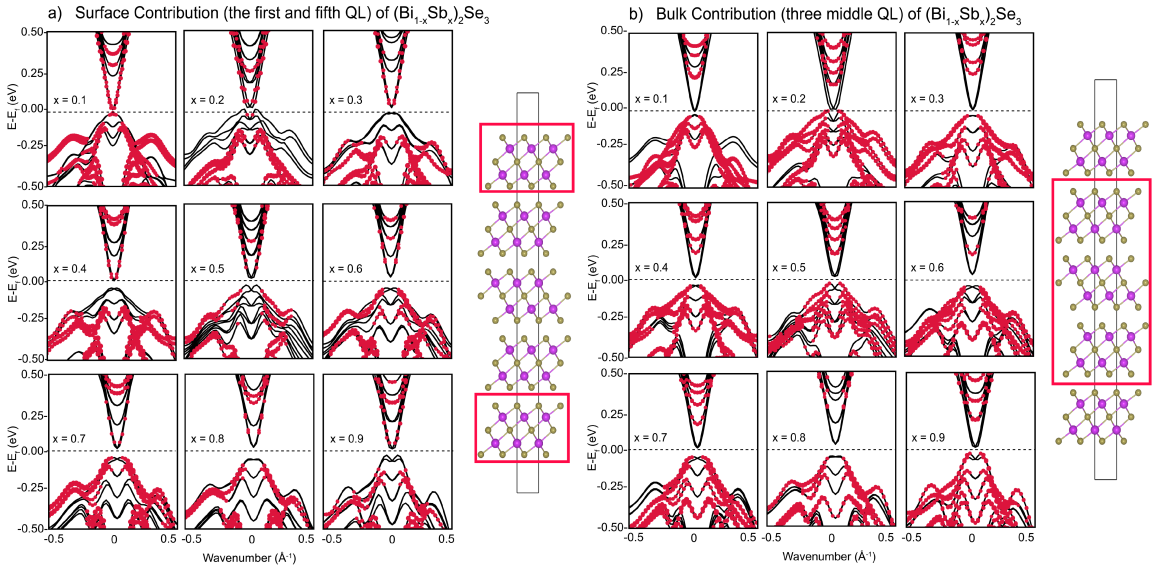

Figure S9. Orbital-weighted electronic band structures of $(Bi_{1-x}Sb_x)_2Se_3$ for Sb compositions ranging from $x = 0.1$ to 0.9 in steps of 0.1. (a) Surface-state contributions originating from the top and bottom QLs. (b) Bulk-state contributions from the three middle QLs. Red markers highlight the states with dominant surface or bulk character, as shown schematically on the right. The observed band evolution with increasing x reveals the gradual modification of surface–bulk separation and the weakening of topological surface states at high Sb content.